PCCP

ROYAL SOCIETY OF CHEMISTRY

PAPER

View Article Online
View Journal | View Issue

Cite this: *Phys. Chem. Chem. Phys.*, 2024, **26**, 26277

Dissociative ionization and post-ionization alignment of aligned O_2 in an intense femtosecond laser field

Shinichi Fukahori, [ab] Ayumi Kubo[a] and Hirokazu Hasegawa *[ab]

Received 19th July 2024,
Accepted 29th September 2024

DOI: 10.1039/d4cp02857k

rsc.li/pccp

We examined dissociative ionization of O_2 in an intense femtosecond laser field (782 nm, 120 fs, 4×10^{14} W cm^{-2}) by recording the kinetic energy distribution of O^+ emitted along the laser polarization direction as a function of the delay time between the pump pulse (9×10^{13} W cm^{-2}) for the molecular alignment and the probe pulse for the dissociative ionization. We found the two distinct rotational revival patterns which are out-of-phase by π with each other in the kinetic energy distribution of O^+. One of the patterns shows the dissociative ionization is enhanced when the O_2 axis is parallel to the laser polarization direction, suggesting that the ionization is induced by the electron emission from the $3\sigma_g$ orbital. On the other hand, the other pattern shows that the dissociative ionization is enhanced when the O_2 axis is perpendicular to the laser polarization direction, suggesting that the ionization is induced by the electron emission from the $1\pi_u$ orbital. Because of the collection efficiency of the time-of-flight mass spectrometer, the enhancement of the O^+ yield at the anti-alignment time delay indicates that the electron emission from the $1\pi_u$ orbital is followed by the molecular alignment of O_2^+ in the course of the dissociation. We performed classical trajectory Monte-Carlo simulation of O_2^+ with the dissociation and rotational coordinates in the light-dressed potential to evaluate the effect of the post-ionization alignment by the probe pulse.

1 Introduction

When molecules are irradiated with an intense laser field, ionization is induced and the electronic states of the molecular ion are coupled to each other by the subsequent laser field.[1,2] Although the bound electronic states of the molecular ion are created at the moment of the electron emission, dissociation of the molecular ion can be induced through the laser-induced electronic state coupling. For example, dissociative ionization of the simplest molecule, H_2, in intense laser fields has been investigated extensively.[3–12] Upon the ionization of H_2, an electron is emitted from the $1\sigma_g$ orbital, resulting in the generation of the ground X $^2\Sigma_g^+$ state, from which the dissociation does not occur. However, the X $^2\Sigma_g^+$ state is coupled to the excited A $^2\Sigma_u^+$ state by the subsequent laser field after the electron emission, leading to the dissociation. This mechanism of dissociation has been understood using the light-dressed potential picture[8,10] and is known as processes such as "bond softening"[4] and "above-threshold dissociation".[3]

Meanwhile, in the case of a many-electron system, it is possible that an electron is emitted from inner-valence orbitals upon ionization.[13–19] Therefore, identification of the molecular orbital from which the electron is emitted is important to understand the ionization dynamics of molecules. The shape of the molecular orbital can be discussed on the basis of the tunnel ionization probability sensitively dependent on the angle between the molecular axis and the laser polarization axis.[20–34] Previously, we examined the angle-dependent probability of the non-dissociative ionization of C_2H_2,[28] NO,[32] and H_2O[33,34] molecules in intense laser fields by recording the molecular ion yield as a function of the time delay between a pair of intense femtosecond laser pulses. In those experiments, the rotational wave packet of the target molecules was created through impulsive rotational Raman transition[35–38] by the pump pulse while the molecule was ionized by the probe pulse, and the produced molecular ions were detected by a time-of-flight mass spectrometer (TOF-MS). Because ionization probability depends on the angle between the molecular axis and the polarization direction, *i.e.*, the molecular alignment angle, the recorded ion yield varies depending on the time delay between the pump and probe pulses associated with the time

[a] *Department of Integrated Sciences, Graduate School of Arts and Sciences, The University of Tokyo, 3-8-1 Komaba, Meguro-ku, Tokyo 153-8902, Japan. E-mail: chs36@mail.ecc.u-tokyo.ac.jp*
[b] *Komaba Institute for Science, Graduate School of Arts and Sciences, The University of Tokyo, 3-8-1 Komaba, Meguro-ku, Tokyo 153-8902, Japan*

evolution of the rotational wave packet. On the basis of a similar technique, the angle-dependent probability of the dissociative ionization of C_2H_2 was examined by the momentum imaging of the fragment ions.[27,39]

Dissociative ionization of O_2 in intense laser fields has been examined extensively,[40–44] because it is also a good example of the laser induced electronic state coupling in the molecular ion after the electron emission. The kinetic energy release (KER) spectra of O^+ in the (1,0) dissociation ($O_2^+ \rightarrow O^+ + O$) exhibit distinct structures, suggesting a variety of dissociative channels. The electron configuration of an O_2 molecule in the ground X $^3\Sigma_g^-$ state is expressed as $(1\sigma_g)^2(1\sigma_u)^2(2\sigma_g)^2(2\sigma_u)^2$-$(3\sigma_g)^2(1\pi_u)^4(1\pi_g)^2$. When an electron is emitted from the highest occupied molecular orbital (HOMO), $1\pi_g$, the ground X $^2\Pi_g$ state of O_2^+ is created, and the ionization probability is found to be enhanced when θ is about 45°, where θ is the angle between the O_2 molecular axis and the laser polarization direction, reflecting the shape of the $1\pi_g$ orbital.[22,24,31] However, the preparation of the deeply bound X $^2\Pi_g$ state has not been considered to be the major origin of the dissociation of O_2^+ in an intense near-infrared laser field.

On the other hand, when an electron is emitted from the HOMO−1, $1\pi_u$, in an intense laser field, the a $^4\Pi_u$ state of O_2^+ is created because the ionization energy (16.7 eV) to the quartet a $^4\Pi_u$ state is lower than that (17.7 eV) to the doublet A $^2\Pi_u$ state.[45] Similarly, when an electron is emitted from the HOMO−2, $3\sigma_g$, the b $^4\Sigma_g^-$ state of O_2^+ is created. Previously, the momentum images of O^+ produced in the dissociation processes from O_2^+ were examined on the basis of the light-dressed potential picture[40] and the a $^4\Pi_u$ state of O_2^+ was found to be the major origin of the dissociation. These assignments with the a $^4\Pi_u$ state were further confirmed by examination of the dissociation of O_2^+ in intense laser fields using an O_2^+ ion beam source as a target sample.[46,47] Meanwhile, from the molecular frame photoelectron angular distributions produced in a circularly polarized laser field,[43] it was recently found that not only electron emission from the $1\pi_u$ orbital but also electron emission from the $3\sigma_g$ orbital can result in dissociation.

The electron emission from the $1\pi_u$ and $3\sigma_g$ orbitals can be distinguished if the delay dependence of the O^+ yield associated with the time evolution of the rotational wave packet of O_2 is examined by the pump–probe method as described above. However, in the experiment with the TOF-MS, a pinhole needs to be installed in front of a micro-channel plate (MCP) detector to obtain KER from TOF, indicating that this method may not be extended from the measurement of the molecular ion to that of the fragment ion in a KER-resolved manner. When the O_2 axis is aligned along the TOF axis, the O^+ fragment ion passes the pinhole and can be detected. On the other hand, when the O_2 axis is anti-aligned, it is considered that the O^+ ion does not pass the pinhole and cannot be detected. Thus, the recorded delay dependence of the O^+ ions may represent only the molecular axis distribution rather than the angular dependence of the dissociative ionization probability, due to the collection efficiency of the detection system.

We solve this problem by using a 120-fs-long pulse as the probe. The O^+ ions produced from anti-aligned O_2 at the moment of ionization can be detected by the effect called post-ionization alignment (PIA), that is, the molecular alignment induced by the laser field after the ionization.[48] In a previous study,[42] the PIA was observed for the 25-fs-long pulse as the peak shift in the angular distribution of O^+ towards the laser polarization direction when the laser-field intensity was increased. Therefore, the duration of 120 fs is sufficiently long to induce the PIA so that O^+ passes the pinhole in the TOF-MS, and we can distinguish the electron emission from the $1\pi_u$ and $3\sigma_g$ orbitals in the various dissociation channels. In this work, we investigate dissociative ionization of O_2 on the basis of the angle-dependent ionization probability by recording the O^+ fragment ion yield as a function of the pump–probe delay.

2 Methods

2.1 Experiment

A linearly polarized femtosecond laser pulse (782 nm, 120 fs, 10 mJ per pulse, 10 Hz) from a Ti:sapphire amplifier (α-10, BM Industries) was split into the pump and probe pulses by a Michelson interferometer. The delay time between the pump and probe pulses was controlled by a linear motorized stage located in the optical path of the probe pulse in the interferometer. The pump and probe pulses were focused on the supersonic molecular beam of O_2 diluted in He (1%, 0.3 MPa) in a vacuum chamber equipped with a TOF-MS by a plano-convex lens (f = 200 mm). The space charge effect can securely be neglected due to the low concentration of O_2 and the high ionization energy of the buffer He gas. The diameter and pulse energy of the pump pulse were adjusted by an iris. We recorded an image of the focal spot by a CMOS camera and the focal diameters of the pump and probe pulses were obtained as 80 μm and 47 μm, respectively. The polarization direction of the two pulses was set to be parallel to the TOF axis and the laser-field intensities at the focal point are estimated to be 9.3×10^{13} W cm^{-2} and 3.9×10^{14} W cm^{-2} for the pump and probe pulses, respectively. In the TOF-MS, an electrode with a pinhole diameter of 5 mm was located in front of a MCP detector so that only O^+ ions emitted along the TOF axis were detected. The acceptance angles are estimated to be ±14° for the released kinetic energy of 1.0 eV and ±5.5° for 7.0 eV. The released kinetic energies were obtained from the difference in the TOF between the forward and backward emission of O^+ and the static electric field strength applied by the electrodes in the TOF-MS.[49]

2.2 Classical trajectory simulation

The effect of the PIA induced by the probe pulse was examined by the classical trajectory Monte-Carlo (CTMC) simulation. The alignment angle distribution of O_2^+ in the a $^4\Pi_u$ or b $^4\Sigma_g^-$ state with respect to the laser polarization direction was initially prepared at the time of the electron emission in the laser pulse on the basis of the angle-dependent ionization probability. The dissociation of O_2^+ was induced by the laser-induced electronic state coupling, and in this simulation, we only consider the

dissociation channels in which only one electronic state is coupled to the initial a $^4\Pi_u$ or b $^4\Sigma_g^-$ state, for simplicity. The change from the initial alignment angle distribution to the distribution after the dissociation was evaluated by the classical trajectory calculation incorporated with the light-dressed potential picture.

In the CTMC simulation, the initial parameters at the time of the electron emission (t_0) were chosen so that their distributions assumed as follows are reproduced. The initial parameters are t_0, the initial internuclear distance of O_2 (r_0), the initial momentum along the molecular axis (p_0), the initial polar and azimuthal angles of the O_2^+ molecular axis with respect to the laser polarization direction (θ_0, φ_0), and the initial angular momenta ($J_{\theta_0}, J_{\varphi_0}$) conjugated to ($\theta_0$, φ_0).

Before ionization, O_2 is in the vibronic ground state X $^3\Sigma_g^-$ (v = 0), suggesting that the Wigner distribution function[50] can be given by the product of the distribution function of the internuclear distance r_0 [$P_{v=0}(r_0)$] and that of the momentum p_0 [$P_p(p_0)$]. In addition, we assumed the isotropic molecular axis distribution of O_2 in a thermal ensemble. The ionization probability was calculated from the cycle-averaged ionization rate $W(r_0,\theta_0,t_0)$ at $t = t_0$, $r = r_0$ and $\theta = \theta_0$ obtained on the basis of the molecular Ammosov–Delone–Krainov (MO-ADK) theory.[51] The expansion coefficients in the MO-ADK theory were set to be C_1 = 2.04, C_3 = 0.33, and C_5 = 0.01 for the $1\pi_u$ orbital and C_0 = 3.05, C_2 = 1.59, and C_4 = 0.08 for the $3\sigma_g$ orbital.[52] To calculate $W(r_0,\theta_0,t_0)$, the ionization energy depending on the internuclear distance of O_2, r, was taken to be the field-free potential energy obtained later in Fig. 6.

Firstly, t_0 was chosen from the distribution according to the ionization rate averaged over r_0 and θ_0 as

$$P_t(t_0)\mathrm{d}t_0 = \frac{\int_0^{\pi}\left[\int_0^{\infty} P_{v=0}(r_0)\,W(r_0,\theta_0,t_0)\mathrm{d}r_0\right]\sin\theta_0\mathrm{d}\theta_0}{\int_0^{\pi}\sin\theta_0\mathrm{d}\theta_0}\mathrm{d}t_0. \quad (1)$$

Secondly, r_0 was chosen from the distribution as

$$P_r(r_0;t_0)\mathrm{d}r_0 = \frac{\int_0^{\pi} P_{v=0}(r_0)\,W(r_0,\theta_0,t_0)\sin\theta_0\mathrm{d}\theta_0}{\int_0^{\pi}\sin\theta_0\mathrm{d}\theta_0}\mathrm{d}r_0, \quad (2)$$

where the product of the Wigner distribution $P_{v=0}(r_0)$ and ionization rate at $t = t_0$ associated with r_0-dependent ionization energy is averaged over θ_0. Thirdly, p_0 was chosen from the Wigner distribution $P_p(p_0)$. Fourthly, θ_0 was chosen from the axis distribution calculated from the ionization rate at $t = t_0$ and $r = r_0$ as

$$P_\theta(\theta_0;t_0,r_0)\sin\theta_0\mathrm{d}\theta_0 = W(r_0,\theta_0,t_0)\sin\theta_0\mathrm{d}\theta_0, \quad (3)$$

while φ_0 was chosen from the uniform distribution. Finally, ($J_{\theta_0}, J_{\varphi_0}$) were chosen according to the Boltzmann distribution[53] of the X $^3\Sigma_g^-$ state (v = 0) of O_2. The initial conditions (t_0,r_0) chosen in the CTMC simulation for the electron emission from the $1\pi_u$ orbital are shown in Appendix A.

Using these initial conditions, we calculated the classical trajectory on the basis of the equation of motion (EOM) as[42,53,54]

$$\begin{cases} \ddot{r} = -\dfrac{1}{\mu}\dfrac{\partial V(r,\theta,t)}{\partial r} \\ \ddot{\theta} = -\dfrac{\Delta\alpha}{4I}[\varepsilon(t)]^2\sin 2\theta - \dfrac{\dot{I}}{I}\dot{\theta} + \dfrac{1}{2}\dot{\varphi}^2\sin 2\theta - \dfrac{1}{I}\dfrac{\partial V(r,\theta,t)}{\partial\theta}, \\ \ddot{\varphi} = -\left(\dfrac{\dot{I}}{I} + \dfrac{2\dot{\theta}}{\tan\theta}\right)\dot{\varphi} \end{cases} \quad (4)$$

where φ is the azimuthal angle, μ is the reduced mass, I is the moment of inertia, $\Delta\alpha = \alpha_\parallel - \alpha_\perp$, $\alpha_\parallel$ and $\alpha_\perp$ are components of the polarizability parallel and perpendicular, respectively, to the molecular axis, and $\varepsilon(t)$ is the laser electric field envelope. In this calculation, the light-dressed potential energy curves $V(r,\theta,t)$ were obtained by the quasi-stationary Floquet approach.[55] The non-diagonal element representing the one-photon parallel transition in the Floquet matrix is expressed as

$$v_1(r,\theta,t) = \frac{1}{2}\mu_t(r)\varepsilon(t)\cos\theta, \quad (5)$$

where $\mu_t(r)$ is the transition dipole moment as a function of r, and the non-diagonal element representing the three-photon parallel transition is expressed as

$$v_3(r,\theta,t) = \frac{1}{2}\beta_t[\varepsilon(t)]^3\cos^3\theta, \quad (6)$$

where β_t is a proportional coefficient. The EOM (4) was solved on the light-dressed potentials $V(r,\theta,t)$ obtained by the diagonalization of the Floquet matrix. In addition, we obtained $\Delta\alpha$ using $\alpha'_\parallel$ defined as

$$\alpha'_\parallel(r) = \alpha_\parallel(r) - \frac{2[\mu_t(r)]^2}{\Delta V(r)}, \quad (7)$$

in place of $\alpha_\parallel$, where $\Delta V(r)$ is the field-free one-photon transition energy, because the effect of the one-photon transition is redundantly taken into account in the first and fourth terms in the second line of eqn (4), where the first and fourth terms represent the polarizability interaction and the angular dependence of the light-dressed potential, respectively.

The non-adiabatic transition between the two dressed potentials was treated by the surface hopping with an ant-eater method.[56] The probability of the non-adiabatic transition was estimated from the Landau–Zener formula. The alignment angle θ_∞ after the dissociation was obtained as[48]

$$\theta_\infty = \theta(t_*) + \int_{t_*}^{\infty}\dot{\theta}\mathrm{d}t = \theta(t_*) + \frac{J_{\theta,\infty}}{r\mu\dot{r}}, \quad (8)$$

where t_* is the time after the laser–O_2^+ interaction and the angular momentum is converged to the final value of $J_{\theta,\infty}$ at t_*.

3 Results and discussion

3.1 Delay dependence of the TOF spectrum of O^+

Fig. 1(b) shows the recorded delay (τ) dependence of the TOF spectrum around a mass-to-charge ratio of 16, $I(t_{TOF},\tau)$.

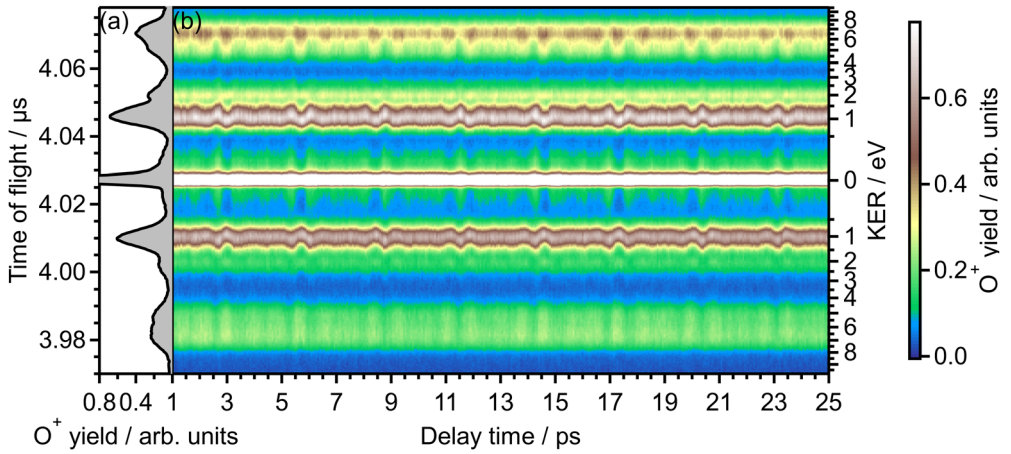

Fig. 1 (a) TOF spectrum for the mass-to-charge ratio of 16 (O^+), obtained only by probe pulse. (b) Delay dependence of the TOF spectrum.

In Fig. 1(a), the TOF spectrum recorded when only the probe pulse is used is also shown. The central strong peak at t_{TOF} = 4.027 μs is assigned to the O_2^{2+} dication produced by the double ionization of O_2 and the delay dependence of the O_2^{2+} yield, as well as that of the O_2^+ yield,[31] is not discussed in this paper. The other peaks are assigned to the O^+ fragment ion and the released kinetic energy E_{KER} is also shown in Fig. 1 on the right axis. The peaks in the energy range of E_{KER} = 0.05–3.5 eV are assigned to O^+ produced in the (1,0) dissociation ($O_2^+ \rightarrow O^+ + O$), while the peaks in the higher energy range are O^+ produced in the (1,1) dissociation ($O_2^{2+} \rightarrow O^+ + O^+$).[40]

In the recorded delay dependence of the TOF spectrum of O^+, the periodic yield modulation can be seen as a function of the delay time between the pump and probe pulses. As discussed later in Section 3.2, this periodic modulation originated from the time evolution of the rotational wave packet of O_2 created by the pump pulse. In particular, for the peak in the range of E_{KER} = 0.5–1.70 eV, the released kinetic energy seems to increase and decrease. However, the kinetic energy may not be varied by the rotational motion of O_2, suggesting that this peak consists of the low energy component and the high energy component whose rotational revival patterns are out-of-phase with each other.

3.2 Fourier transform of the delay-dependent TOF spectrum of O^+

Fig. 2(b) shows the Fourier transform (FT), $\tilde{I}(t_{TOF},\tilde{\nu})$, of the delay-dependent TOF spectrum, $I(t_{TOF},\tau)$, [Fig. 1(b)] with respect to the delay, τ. The FT spectrum exhibits the peaks at the wavenumbers of $\tilde{\nu}$ = $10B_0$, $18B_0$, $26B_0$, $34B_0$, $42B_0$, $50B_0$, where B_0 = 1.43767638 cm^{-1} is the rotational constant of O_2 in the vibrational ground level of $X\ ^3\Sigma_g^-$.[57] These peaks are assigned to be the energy difference $S(N) = (4N + 6)B_0$ between the two rotational levels of O_2 whose rotational angular momentum quantum numbers N differ by 2 (ΔN = 2). Due to the nuclear-spin statistics, N takes only an odd value. Therefore, these

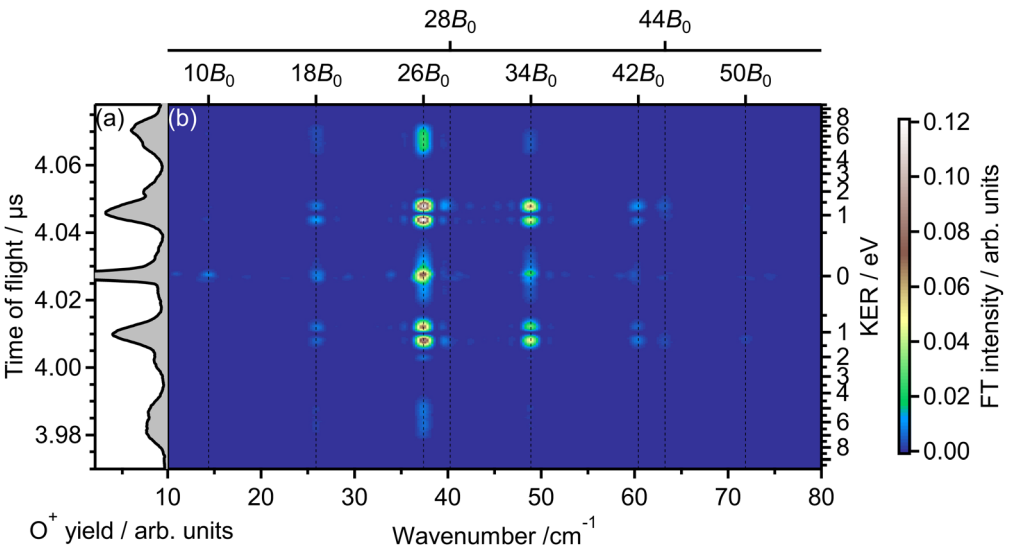

Fig. 2 (a) TOF spectrum for a mass-to-charge ratio of 16 (O^+), obtained only by probe pulse. The same as in Fig. 1(a). (b) Fourier transform of the delay-dependent TOF spectrum.

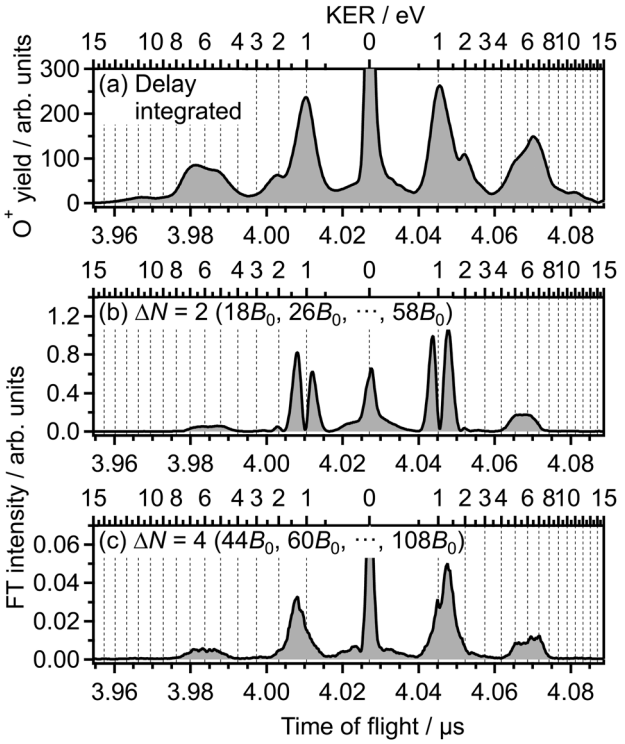

Fig. 3 (a) Delay-integrated TOF spectrum. (b) Frequency-integrated TOF spectrum at $\Delta N = 2$. (c) Frequency-integrated TOF spectrum at $\Delta N = 4$.

peaks in the FT spectrum mean that the yield modulation observed in Fig. 1(b) originates from the time evolution of the rotational wave packet of O_2. Moreover, the FT spectrum exhibits the peaks at $\tilde{\nu} = 28B_0$ and $44B_0$, which are assigned to be the energy difference $U(N) = (8N + 20)B_0$ between the two rotational levels of O_2 with $\Delta N = 4$.

In Fig. 3(a), the delay-integrated TOF spectrum $\tilde{I}_0(t_{TOF})$ is obtained as

$$\tilde{I}_0(t_{TOF}) = \int_{\tau_i}^{\tau_f} I(t_{TOF}, \tau)\mathrm{d}\tau, \quad (9)$$

where $\tau_i = 1$ ps and $\tau_f = 25$ ps is shown and is found to be almost the same as the TOF spectrum obtained when only the probe pulse is used, shown in Fig. 1(a) and 2(a). On the other hand, Fig. 3(b) shows the frequency-integrated TOF spectrum $\tilde{I}_2(t_{TOF})$ defined as

$$\tilde{I}_2(t_{TOF}) = \sum_N \int_{S(N)-\Delta\tilde{\nu}}^{S(N)+\Delta\tilde{\nu}} \tilde{I}(t_{TOF}, \tilde{\nu})\mathrm{d}\tilde{\nu}, \quad (10)$$

where the summation was performed over all the $\Delta N = 2$ peaks and $\Delta\tilde{\nu}$ is set to be the typical frequency resolution of the FT, $1/(\tau_f - \tau_i) = 1.39\ \mathrm{cm}^{-1}$. The frequency-integrated TOF spectrum $\tilde{I}_2(t_{TOF})$ exhibits the different spectral shape from the delay-integrated TOF spectrum. For example, the peak at $E_{KER} = 1.03$ eV in Fig. 3(a) is divided into two peaks at $E_{KER} = 0.84$ and 1.32 eV in Fig. 3(b). The frequency-integrated TOF spectrum $\tilde{I}_4(t_{TOF})$ is also obtained as

$$\tilde{I}_4(t_{TOF}) = \sum_N \int_{U(N)-\Delta\tilde{\nu}}^{U(N)+\Delta\tilde{\nu}} \tilde{I}(t_{TOF}, \tilde{\nu})\mathrm{d}\tilde{\nu}, \quad (11)$$

where the summation was performed over all the $\Delta N = 4$ peaks, and is shown in Fig. 3(c). From these TOF spectra, five channels in the (1,0) dissociation are identified as the energy ranges I (E_{KER} = 0.05–0.40 eV), II (0.50–1.04 eV), III (1.04–1.70 eV), IV (1.80–2.40 eV) and V (2.40–3.40 eV). Each delay dependence of the O^+ yield is obtained as

$$Y_X(\tau) = \int_{t_{2,X}^{fwd}}^{t_{1,X}^{fwd}} I(t_{TOF}, \tau)\mathrm{d}t_{TOF} + \int_{t_{1,X}^{bwd}}^{t_{2,X}^{bwd}} I(t_{TOF}, \tau)\mathrm{d}t_{TOF}, \quad (12)$$

where X = I, II, III, ... is the label of the energy range from $E_{KER} = E_{1,X}$ to $E_{KER} = E_{2,X}$ and $t_{i,X}^{fwd}$ and $t_{i,X}^{bwd}$ are the time-of-flight corresponding to $E_{KER} = E_{i,X}$ ($i = 1, 2$) for the forward and backward emission of O^+, respectively, with respect to the direction towards the MCP detector, and will be discussed in the next subsection.

3.3 Delay dependence of O^+ yield for (1,0) dissociation

3.3.1 Energy range I (0.05–0.40 eV). Fig. 4(a) shows the O^+ yield, $Y_I(\tau)$, as a function of the delay time in the lowest energy range I. In Fig. 4(f), the energy ranges are depicted with the TOF spectrum obtained only by the probe pulse. The O^+ yield exhibits the increase and decrease periodically and the period is the rotational period of O_2, $T_{rot} = 1/(2cB_0)$, where c is the speed of light. We numerically solved the time-dependent Schrödinger equation in which the effect of the electron spin is taken into account[58] to calculate the time evolution of the rotational wave packet of O_2 created by the pump pulse. Fig. 5(a) shows the calculated expectation value $\langle\langle\cos^2\theta\rangle\rangle$ of $\cos^2\theta$ as a function of time t where θ is the alignment angle of the O_2 axis with respect to the laser polarization direction and the expectation value is averaged over the initial rotational state distribution at 7.5 K. The estimation of the rotational temperature of 7.5 K will be discussed later in Section 3.3.2. When the O_2 axis is aligned along the laser polarization direction, $\langle\langle\cos^2\theta\rangle\rangle$ becomes close to 1, while when the O_2 axis is anti-aligned, $\langle\langle\cos^2\theta\rangle\rangle$ becomes close to 0. We found that the experimental O^+ yield is out-of-phase with $\langle\langle\cos^2\theta\rangle\rangle(t)$. The O^+ yield increases when the O_2 axis is anti-aligned with respect to the laser polarization direction. This result suggests that O^+ in the energy range I is produced when an electron is emitted from the $1\pi_u$ orbital.

We also calculated the yield of ionization corresponding to the electron emission from the $1\pi_u$ orbital as a function of the pump–probe delay on the basis of the MO-ADK theory as in ref. 32. The delay dependence of the calculated ionization yield is shown in Fig. 5(b) and the yield increases when $\langle\langle\cos^2\theta\rangle\rangle$ decreases in Fig. 5(a). Therefore, it is confirmed that the observed revival pattern in the energy range I [Fig. 4(a)] which is out-of-phase with $\langle\langle\cos^2\theta\rangle\rangle(t)$ represents the electron emission from the $1\pi_u$ orbital.

As discussed in the introduction, the a $^4\Pi_u$ state is considered to be created at the moment of the electron emission from

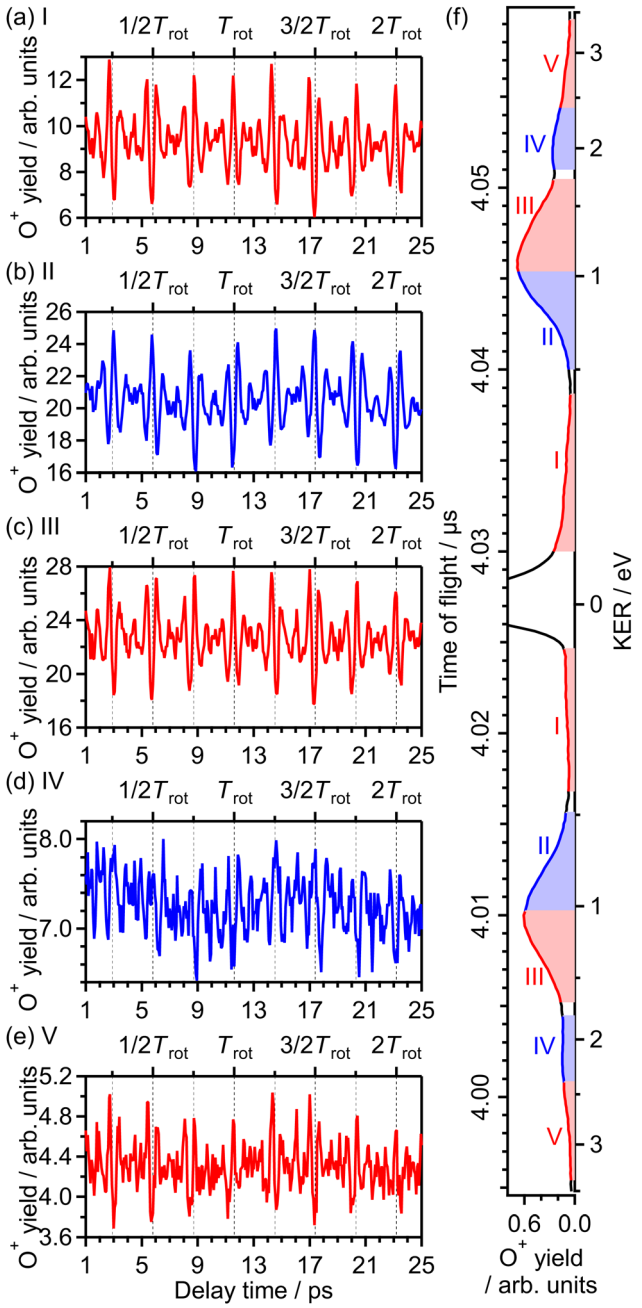

Fig. 4 Recorded O^+ yields as a function of delay time in the energy ranges (a) I, (b) II, (c) III, (d) IV and (e) V. (f) TOF spectrum obtained only by the probe pulse [same as Fig. 1(a)] with the labels of the energy ranges I, II, III, IV and V.

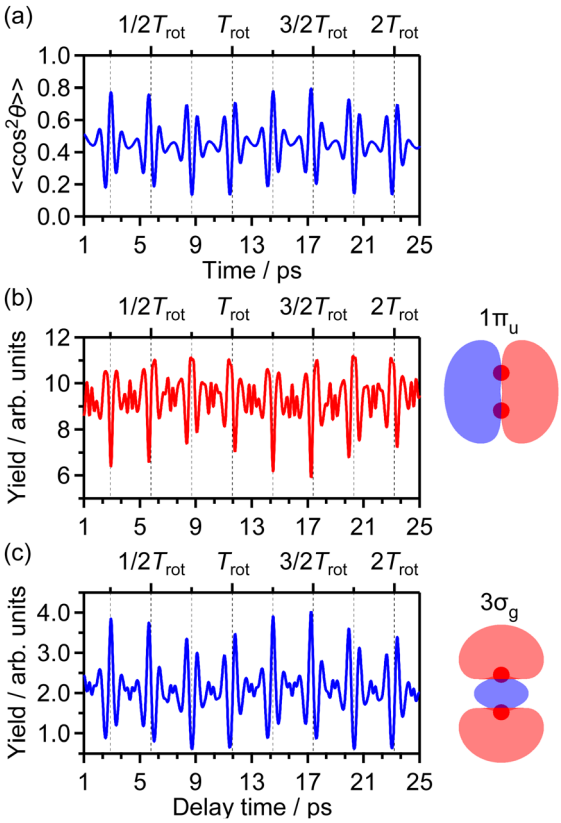

Fig. 5 (a) $\langle\langle\cos^2\theta\rangle\rangle(t)$. (b) O^+ yield calculated by MO-ADK with $1\pi_u$ (inset). (c) O^+ yield calculated by MO-ADK with $3\sigma_g$ (inset). The pump and probe intensities are set to be 3.3×10^{13} W cm^{-2} and 1.4×10^{14} W cm^{-2}, respectively, and the rotational temperature is set to be 7.5 K.

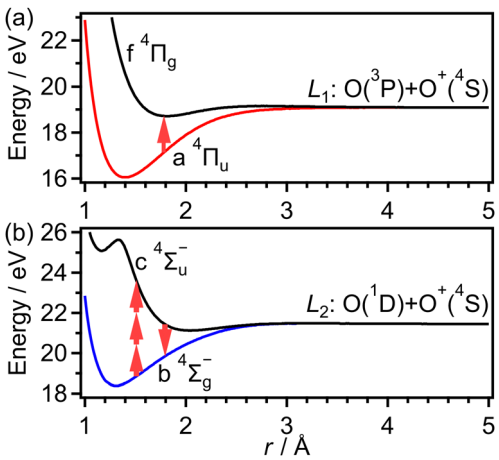

Fig. 6 Potential energy curves of (a) a $^4\Pi_u$ and f $^4\Pi_g$ states and (b) b $^4\Sigma_g^-$ and c $^4\Sigma_u^-$ states.

the $1\pi_u$ orbital. The lowest energy range I has been assigned to O^+ produced in the bond softening associated with f $^4\Pi_g$–a $^4\Pi_u$ one-photon crossing followed by the dissociation into the dissociation limit called L_1 as[41,46,47]

$$O_2^+(a\ ^4\Pi_u) \xrightarrow{1\omega} O_2^+(f\ ^4\Pi_g) \rightarrow O(^3P) + O^+(^4S), \qquad (13)$$

which is depicted in Fig. 6(a). In Fig. 6, the potential energy curves of O_2^+ are obtained by the quantum chemical calculation using GAMESS 2018 R1[59] at the MCSCF/aug-cc-pVTZ level followed by the configuration interaction calculation with the graphical unitary group approach (GUGA).[60] The rotational revival pattern observed in Fig. 4(a) agrees with these previous assignments of the ionization to the a $^4\Pi_u$ state.

3.3.2 Energy range II (0.50–1.04 eV). Fig. 4(b) shows the O^+ yield $Y_{II}(\tau)$ in the energy range II which is the lower energy side

of the peak at E_{KER} = 1.03 eV as shown in Fig. 4(f). Similarly to Fig. 4(a), the O^+ yield in the energy range II exhibits the periodic decrease and increase. However, the O^+ yield is in-phase with the calculated $\langle\langle\cos^2\theta\rangle\rangle(t)$ shown in Fig. 5(a). This result means that the O^+ yield increases when the O_2 axis is aligned along the laser polarization direction and suggests that O^+ in the energy range II is produced when an electron is emitted from the $3\sigma_g$ orbital.

The O^+ yield calculated on the basis of the MO-ADK theory for the $3\sigma_g$ orbital is shown in Fig. 5(c). We found that the rotational revival pattern in the calculated O^+ yield agrees well with that in the experimental O^+ yield and confirmed that the energy range II is associated with the electron emission from the $3\sigma_g$ orbital. We note that the pump and probe laser-field intensities of 3.3 × 10^{13} W cm^{-2} and 1.4 × 10^{14} W cm^{-2}, respectively, and the rotational temperature of 7.5 K are adopted for the calculation so that the discrepancy between the calculated O^+ yield shown in Fig. 5(c) and the observed O^+ yield shown in Fig. 4(b) is minimized.[33]

As discussed in the introduction, the b $^4\Sigma_g^-$ state is considered to be created at the moment of the electron emission from the $3\sigma_g$ orbital. The O^+ ions in the range of E_{KER} = 0.50–1.04 eV can be generated by the dissociation of O_2^+ into the dissociation limit called L_2 by the net-two photon absorption from the b $^4\Sigma_g^-$ state. Indeed, when the vibrational levels of v^+ = 0 and 1 in b $^4\Sigma_g^-$ of O_2^+ are prepared at the moment of the electron emission, the absorption of two 782-nm-wavelength photons (1.59 eV) results in E_{KER} = 0.64 and 0.79 eV, respectively, obtained from the ionization energies (18.17 eV for v^+ = 0 and 18.31 eV for v^+ = 1)[61] and the energy of the L_2 limit (20.70 eV).[62] We consider that the energy range II can be assigned to O^+ produced in the net-two photon dissociation into the L_2 limit associated with c $^4\Sigma_u^-$–b $^4\Sigma_g^-$ three-photon and one-photon crossings as

$$O_2^+\left(b\,^4\Sigma_g^-\right) \xrightarrow{3\omega} O_2^+\left(c\,^4\Sigma_u^-\right) \xrightarrow{-\omega} O_2^+\left(b\,^4\Sigma_g^-\right) \rightarrow O(^1D) + O^+(^4S), \quad (14)$$

which is depicted in Fig. 6(b).

3.3.3 Energy range III (1.04–1.70 eV). Fig. 4(c) shows the O^+ yield $Y_{III}(\tau)$ in the energy range III which is the higher energy side of the peak at E_{KER} = 1.03 eV as shown in Fig. 4(f). The observed rotational revival pattern in the range III is found to be out-of-phase with $\langle\langle\cos^2\theta\rangle\rangle(t)$ shown in Fig. 5(a), while in-phase with that in the lowest energy range I. This means that O^+ in this energy range III is produced when an electron is emitted from the $1\pi_u$ orbital, that is, the ionization to the a $^4\Pi_u$ state. Thus, the peak at E_{KER} = 1.03 eV is composed of the two different ionization pathways to the a $^4\Pi_u$ and b $^4\Sigma_g^-$ states, resulting in the increase and decrease in E_{KER} shown in Fig. 1(b).

In previous studies,[40,42,46] many assignments are proposed as the dissociation pathways in this energy range of E_{KER} = 1.04–1.70 eV from the a $^4\Pi_u$ state, which agrees with the rotational revival pattern observed in Fig. 4(c). One of the candidates of the dissociation pathway is two photon excitation to the 1 $^4\Sigma_u^+$ state followed by the dissociation into the L_1 limit.[42,46] This pathway corresponds to the above-threshold dissociation (ATD) of the energy range I. Indeed, the energy difference between the ranges I and III is close to the one photon energy (1.59 eV). On the other hand, direct or sequential three photon excitation to the 2 $^4\Pi_g$ state followed by the dissociation into the L_2 limit is also known as a possible candidate.[40,46]

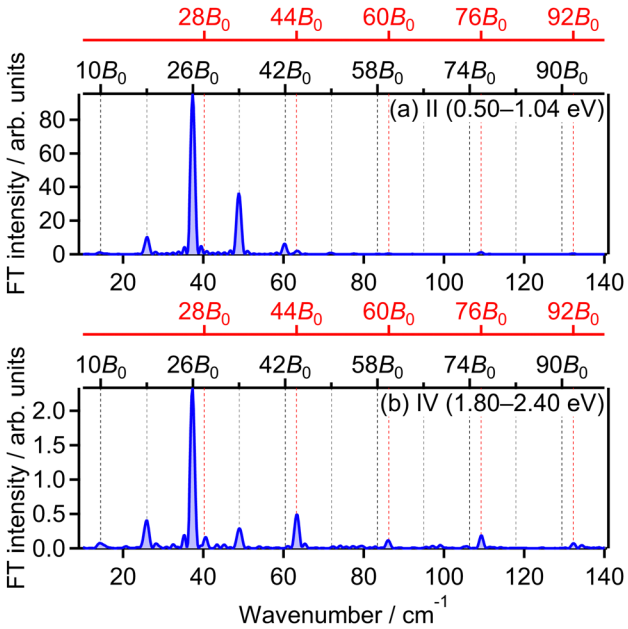

Fig. 7 Fourier transform of O^+ yield in energy ranges (a) II and (b) IV.

3.3.4 Energy range IV (1.80–2.40 eV). Fig. 4(d) shows the O^+ yield $Y_{IV}(\tau)$ in the energy range IV which is a shoulder-like structure as shown in Fig. 4(f). The observed rotational revival pattern in the energy range IV is found to be in-phase with both of $\langle\langle\cos^2\theta\rangle\rangle(t)$ shown in Fig. 5(a) and that in the energy range II. This means that O^+ in this energy range IV is produced when an electron is emitted from the $3\sigma_g$ orbital, that is, the ionization to the b $^4\Sigma_g^-$ state.

Considering that the energy difference between the ranges II (0.50–1.04 eV) and IV (1.80–2.40 eV) is close to the one photon energy, the energy range IV can be assigned to the ATD of the range II. In other words, the dissociation into the L_2 limit is followed by net-three photon absorption from the b $^4\Sigma_g^-$ state. This process is achieved when the one photon emission does not occur in Fig. 6(b), that is, nonadiabatic transition at c $^4\Sigma_u^-$–b $^4\Sigma_g^-$ one-photon crossing in the light-dressed potential picture. Therefore, we assign this energy range IV to the three-photon ATD as

$$O_2^+\left(b\,^4\Sigma_g^-\right) \xrightarrow{3\omega} O_2^+\left(c\,^4\Sigma_u^-\right) \rightarrow O(^1D) + O^+(^4S). \quad (15)$$

In order to evaluate the similarity in the delay dependence of the O^+ yield in the two different energy ranges X_1 and X_2,

we obtain the correlation coefficient as

$$C_{X_1,X_2} = \frac{\sum_i \left[I_{X_1}(\tau_i) - \overline{I_{X_1}(\tau_i)}\right]\left[I_{X_2}(\tau_i) - \overline{I_{X_2}(\tau_i)}\right]}{\sqrt{\sum_i \left[I_{X_1}(\tau_i) - \overline{I_{X_1}(\tau_i)}\right]^2 \sum_i \left[I_{X_2}(\tau_i) - \overline{I_{X_2}(\tau_i)}\right]^2}}. \quad (16)$$

The correlation coefficient $C_{\mathrm{II,IV}}$ is found to be 77%, meaning that the delay dependence of the O^+ yield in the energy range IV is slightly different from that in the range II, even though the electrons are emitted from the same $3\sigma_g$ orbital. This result indicates that not only the dynamics in the electron emission but also the dissociation dynamics are encoded in the observed delay dependence of the O^+ yield. Indeed, the rotational revival structure shown in Fig. 4(d) is less clear than that in Fig. 4(b). Fig. 7(a) and (b) show the FT spectrum of the delay-dependent O^+ yield in the energy range II, $Y_{\mathrm{II}}(\tau)$, and that in the range IV, $Y_{\mathrm{IV}}(\tau)$, respectively. The peaks at $\tilde{\nu} = 28B_0$, $44B_0$, $60B_0$, $76B_0$ and $92B_0$ which are assigned to $\Delta N = 4$ components are found to be enhanced for the energy range IV. These $\Delta N = 4$ frequencies in the energy range IV are the origins of the difference from the range II and the difference between the two FT spectra will be discussed in Section 3.4.2.

3.3.5 Energy range V (2.40–3.40 eV). Fig. 4(e) shows the O^+ yield $Y_{\mathrm{V}}(\tau)$ in the highest energy range V which is the tail-like structure, as shown in Fig. 4(f). The observed rotational revival pattern in the energy range V is found to be out-of-phase with $\langle\langle\cos^2\theta\rangle\rangle(t)$ shown in Fig. 5(a) while in-phase with those in the energy ranges I and III. This means that O^+ in this energy range V is produced when an electron is emitted from the $1\pi_u$ orbital, that is, the ionization to the a $^4\Pi_u$ state. The energy difference between the ranges III (1.04–1.70 eV) and V (2.40–3.40 eV) is close to the one photon energy, indicating that the energy range V can be assigned to the higher-order ATD of the ranges I and III. We note that no assignments of this highest energy range V have been reported in previous studies.

The correlation coefficients for the electron emission from the $1\pi_u$ orbital are obtained as $C_{\mathrm{I,III}} = 97\%$ and $C_{\mathrm{I,V}} = 80\%$. As seen in Fig. 4(a) and (c), the delay dependence of the O^+ yield in the energy range III is very similar to that in the range I. On the other hand, the delay dependence of the O^+ yield in the energy range V shown in Fig. 4(e) is slightly different from that in the range I. Fig. 8(a)–(c) show the FT spectra of the delay-dependent O^+ yield in the energy range I, $Y_{\mathrm{I}}(\tau)$, that in the range III, $Y_{\mathrm{III}}(\tau)$, and that in the range V, $Y_{\mathrm{V}}(\tau)$, respectively. Similarly to the case for the electron emission from the $3\sigma_g$ orbital, the peaks assigned to the $\Delta N = 4$ components are found to be enhanced only for the energy range V.

3.4 Effects of post-ionization alignment

3.4.1 Ionization to the a $^4\Pi_u$ state. The enhancement of the O^+ yield at the anti-alignment cannot be observed as long as the emitting direction of O^+ is parallel to the O_2 axis at the moment of the electron emission due to the pinhole located in front of the MCP detector. It is considered that the O^+ yield increases when the O_2 axis is parallel to the TOF axis, resulting in a similar delay dependence to those in the energy ranges II and VI. However, we observed the yield increase at the anti-alignment in the energy ranges I, III and V. These results indicate that PIA[42,48] is induced by the falling edge of the laser pulse in the course of dissociation so that the O^+ ions can be detected. In order to estimate the extent of the PIA induced by the probe pulse, we performed the CTMC simulation, described in Section 2.2, for the energy range I. As discussed in Section 3.3.1, the a $^4\Pi_u$ state is created associated with the electron emission from the $1\pi_u$ orbital and dissociation is induced by the bond softening by one-photon crossing between f $^4\Pi_g$ and a $^4\Pi_u$ states as in eqn (13).

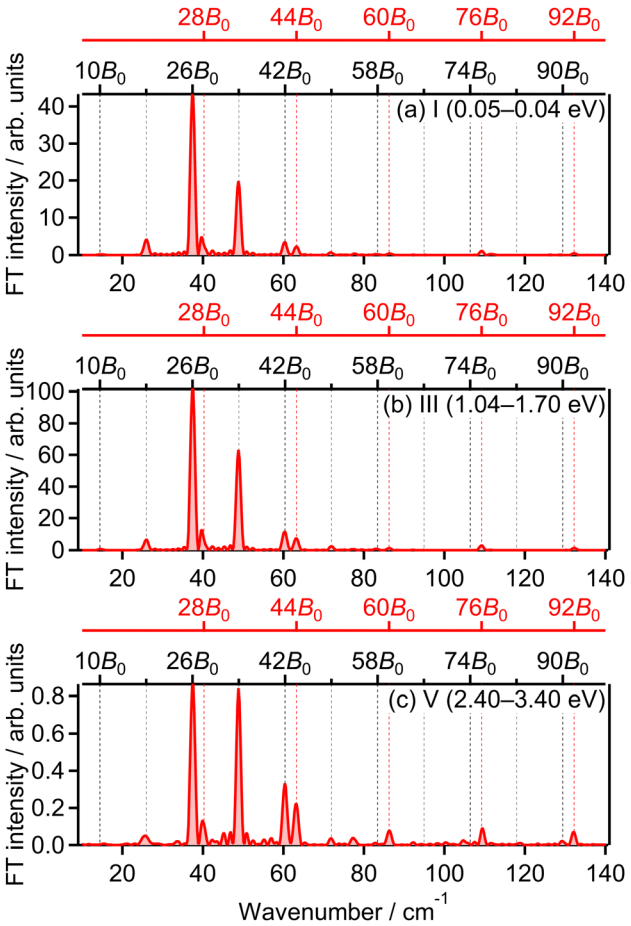

Fig. 8 Fourier transform of O^+ yield in energy ranges (a) I, (b) III and (c) V.

The transition dipole moment between the f $^4\Pi_g$ and a $^4\Pi_u$ states was calculated as a function of r as shown in Appendix B and is parallel to the O_2^+ axis. We also calculated the polarizabilities, $\alpha_\parallel$ and $\alpha_\perp$, of O_2^+ in the a $^4\Pi_u$ state as a function of r by the finite-element method as shown in Appendix B. On the basis of the model suggested in ref. 48, $\alpha'_\parallel(r)$ was obtained as $\alpha'_\parallel(r)\big/\text{a.u.} = 11.50 + 13.21(r - r_e)/a_0$ and $\alpha_\perp(r)$ was obtained as a constant value of $\alpha_\perp(r) = 5.94$ a.u., where $r_e = 1.40$ Å is the equilibrium internuclear distance of O_2^+ in the a $^4\Pi_u$ state and a_0 is the Bohr radius. In this calculation, the same values were used as the polarizabilities of O_2^+ in the f $^4\Pi_g$ state as discussed in Appendix B.

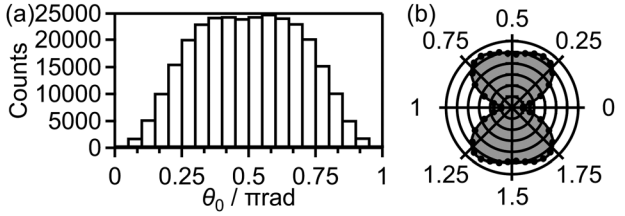

Fig. 9 (a) Distribution $P(\theta_0)\sin\theta_0 d\theta_0$ of the initial alignment angle θ_0 for the electron emission from the $1\pi_u$ orbital. (b) Angle-dependent ionization probability $P(\theta_0)$ obtained from (a). Angular dependence of the ionization rate in the MO-ADK theory at t_0 = 0 and r_0 = 1.208 Å, the equilibrium internuclear distance of O_2 in the X $^3\Sigma_g^-$ state, is also shown as a solid line with a shade.

Fig. 9(a) shows the distribution of the initial alignment angle (θ_0) at the moment of the electron emission from the $1\pi_u$ orbital in the CTMC simulation in which 3×10^5 trajectories were calculated. The corresponding angle-dependent ionization probability shown in Fig. 9(b) agrees with the shape of the $1\pi_u$ orbital shown in the inset of Fig. 5(b). This means that the O_2 axis at the moment of the electron emission from the $1\pi_u$ orbital is anti-aligned with respect to the laser polarization direction. We confirmed that the obtained angle-dependent ionization probability well reproduces the angular dependence of the ionization rate in the MO-ADK theory as shown in Fig. 9(b).

Among all the trajectories, the dissociation occurs for around 1×10^4 trajectories. Fig. 10(a) shows the correlation between θ_0 at the moment of electron emission and θ_∞ after dissociation for the dissociation trajectories. The effect of the PIA can be discussed on the basis of this correlation map. If the classical trajectories are plotted as dots on the diagonal line $\theta_\infty = \theta_0$, the effect of the PIA can be neglected. However, Fig. 10(a) exhibits the tendency of $\theta_\infty < \theta_0$ ($\theta_0 < \pi/2$) or $\theta_\infty > \theta_0$ ($\theta_0 > \pi/2$), indicating that the PIA is induced by the laser field. For example, although θ_0 is initially 0.3π, major trajectories resulted in θ_∞ close to 0, that is, O^+ is emitted along the laser polarization direction. The distributions of θ_0 and θ_∞ for the dissociation trajectories are also shown in Fig. 10(b) and (c), respectively. The θ_0 distribution exhibits peaks at 0.3π and 0.7π while the θ_∞ distribution exhibits peaks at 0 and π. Therefore, we confirm the effect of PIA for the energy range I.

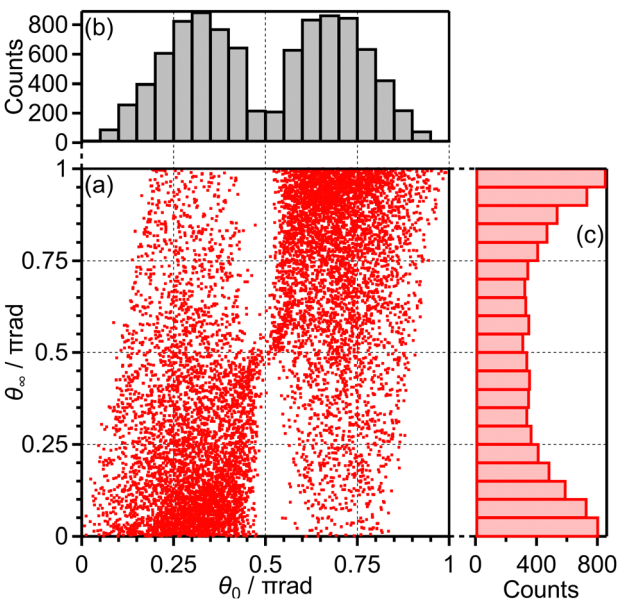

Fig. 10 (a) Correlation between θ_0 and θ_∞, (b) the θ_0 distribution and (c) the θ_∞ distribution for bond softening (energy range I).

Fig. 11(a) shows one of the classical trajectories for which O^+ is emitted along the laser polarization direction though the O_2 axis is anti-aligned at the moment of the electron emission. On the other hand, Fig. 11(b) shows one of the classical trajectories for which the O_2^+ axis rotates further by strong torque induced by the laser field so that O^+ is not emitted along the laser polarization direction. This trajectory resulted in the broad distribution over $\theta_\infty > \theta_0$ ($\theta_0 < \pi/2$) in Fig. 10(a).

3.4.2 Ionization to the b $^4\Sigma_g^-$ state. We also performed similar CTMC simulation for the electron emission from the $3\sigma_g$ orbital. As discussed in Sections 3.3.2 and 3.3.4, at first, O_2^+ is prepared in the b $^4\Sigma_g^-$ state and is excited to the c $^4\Sigma_u^-$ state at the three-photon crossing. If O_2^+ emits one photon at the next one-photon crossing in the light-dressed potential picture, the net-two photon dissociation occurs resulting in the energy range II as in eqn (14). On the other hand, if non-adiabatic transition occurs at the one-photon crossing, the three-photon ATD occurs resulting in the energy range IV as in eqn (15). In contrast to the dipole moment μ_t for the one photon transition, it is hard to obtain a proportional coefficient β_t in the Floquet matrix elements from quantum chemical calculation software packages. In this calculation, β_t/e is set to be 1×10^{-32} m^3 V^{-2}, where e is the elementary charge. We also performed similar simulation with $\beta_t/e = 0.5 \times 10^{-32}$ m^3 V^{-2} and 2×10^{-32} m^3 V^{-2} and confirmed that the consequences derived from the simulation do not sensitively depend on the β_t value except for the dissociation probability.

We calculated 1×10^5 trajectories and the distribution of the initial alignment angle (θ_0) at the moment of the electron emission is shown in Fig. 12(a). The corresponding angle-

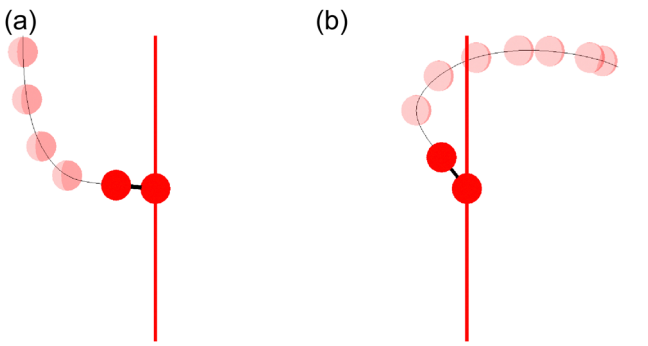

Fig. 11 Classical trajectories for bond softening (energy range I). One of the O atoms is located at the origin and the time variation of the (r,θ,φ) coordinates is depicted as the position of the other O atom. The red vertical line represents the laser polarization direction. (a) θ_0 = 0.47339π. (b) θ_0 = 0.22706π.

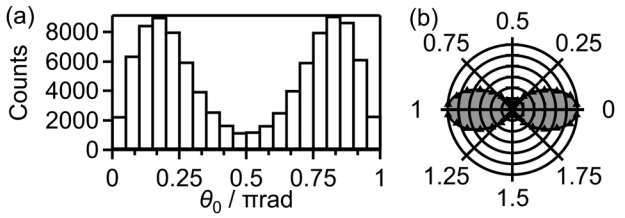

Fig. 12 (a) Distribution $P(\theta_0)\sin\theta_0 d\theta_0$ of the initial alignment angle θ_0 for the electron emission from the $3\sigma_g$ orbital. (b) Angle-dependent ionization probability $P(\theta_0)$ obtained from (a). Angular dependence of the ionization rate in the MO-ADK theory at t_0 = 0 and r_0 = 1.208 Å is also shown as a solid line with a shade.

dependent ionization probability shown in Fig. 12(b) agrees with the shape of the $3\sigma_g$ orbital shown in the inset of Fig. 5(c). This means that the O_2 axis at the moment of the electron emission from the $3\sigma_g$ orbital is aligned along the laser polarization direction.

Among these 1×10^5 trajectories, 8×10^3 trajectories lead to the net-two photon process and other 8×10^3 trajectories lead to the three-photon ATD. Fig. 13(a) shows the angular correlation map for the net-two photon process [eqn (14)]. The correlation map exhibits the tendency of $\theta_\infty < \theta_0$ ($\theta_0 < \pi/2$) or $\theta_\infty > \theta_0$ ($\theta_0 > \pi/2$), suggesting that the O_2^+ axis is more aligned along the laser polarization direction by the PIA effect in the energy range II. On the other hand, Fig. 14(a) shows the correlation map for the three-photon ATD [eqn (15)]. Although the major classical trajectories resulted in $\theta_\infty < \theta_0$ ($\theta_0 < \pi/2$) or $\theta_\infty > \theta_0$ ($\theta_0 > \pi/2$) also for the three-photon ATD, θ_∞ becomes closer to θ_0 than that for the net-two photon dissociation. The change in the O_2^+ axis direction in the energy range IV is considered to be less than that in the energy range II. Therefore, the extent of the PIA depends on the dissociation channels

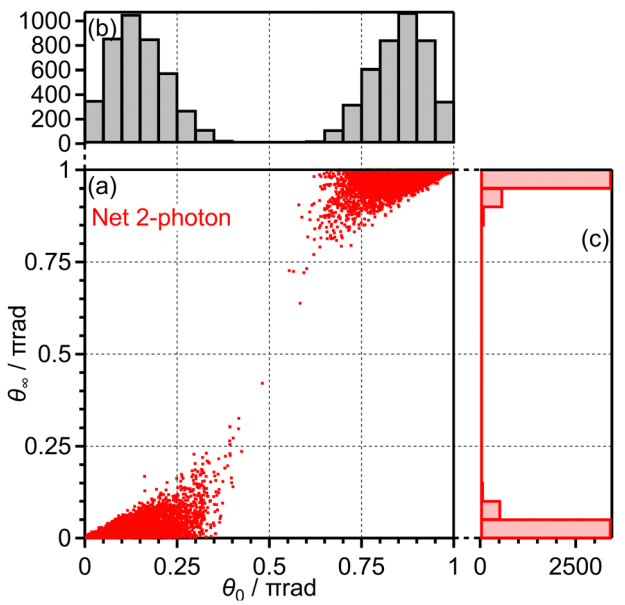

Fig. 13 (a) Correlation between θ_0 and θ_∞, (b) the θ_0 distribution and (c) the θ_∞ distribution for net-two photon dissociation (energy range II).

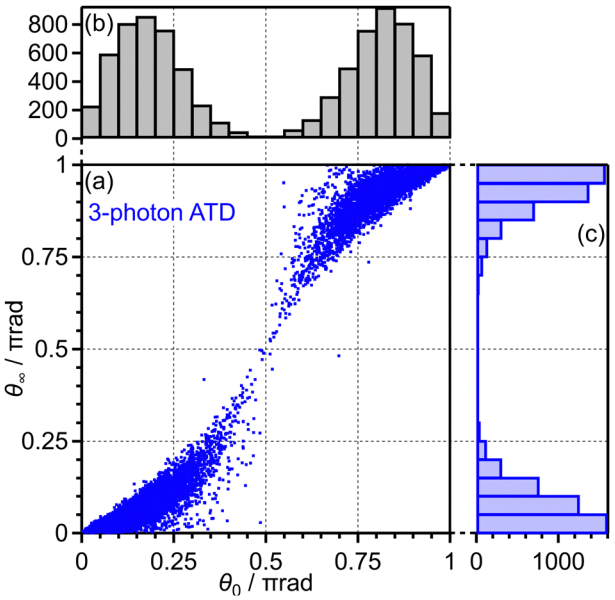

Fig. 14 (a) Correlation between θ_0 and θ_∞, (b) the θ_0 distribution and (c) the θ_∞ distribution for three-photon ATD (energy range IV).

and the θ_∞ distribution, which corresponds to the angular distribution of O^+, can be different even though an electron is emitted from the same $3\sigma_g$ orbital in both of the channels. We consider that this difference in the PIA originates from the difference in the velocity of the dissociation and results in the difference in the FT spectra discussed in Section 3.3.4. Thus, when the PIA effect is small, higher ΔN components appear in the delay dependence of the O^+ yield, reflecting the time evolution of the molecular axis distribution of O_2 rather than the angle-dependent ionization probability.

3.5 Delay dependence of O^+ yield for (1,1) dissociation

As seen in Fig. 1(b), the yield of O^+ produced in the (1,1) dissociation exhibits the periodic increase and decrease as a function of time associated with the time evolution of the rotational wave packet of O_2. Fig. 15(a) shows the O^+ yield $Y_{VI}(\tau)$ in the energy range VI (E_{KER} = 3.60–5.80 eV) which is a lower energy side of the (1,1) dissociation as shown in Fig. 15(c). The observed rotational revival pattern in the energy range VI is found to be in-phase with both of $\langle\langle\cos^2\theta\rangle\rangle(t)$ shown in Fig. 5(a) and that in the energy ranges II and VI. Similarly, Fig. 15(b) shows the O^+ yield $Y_{VII}(\tau)$ in the energy range VII (E_{KER} = 5.80–9.00 eV) which is a higher energy side of the (1,1) dissociation as shown in Fig. 15(c). The observed rotational revival pattern in the energy range VII is found to be also in-phase with $\langle\langle\cos^2\theta\rangle\rangle(t)$. These results indicate that O^+ in the (1,1) dissociation is produced when at least one of two electrons is emitted from the $3\sigma_g$ orbital. It is also possible that, because the (1,1) dissociation rapidly proceeds, the recorded delay dependence represents the axis distribution of O_2 rather than the angular dependence of the ionization probability due to the pinhole located in front of the MCP detector.

The correlation coefficient $C_{II,VI}$ is found to be 87%, suggesting that the (1,1) dissociation in the energy range VI exhibits a

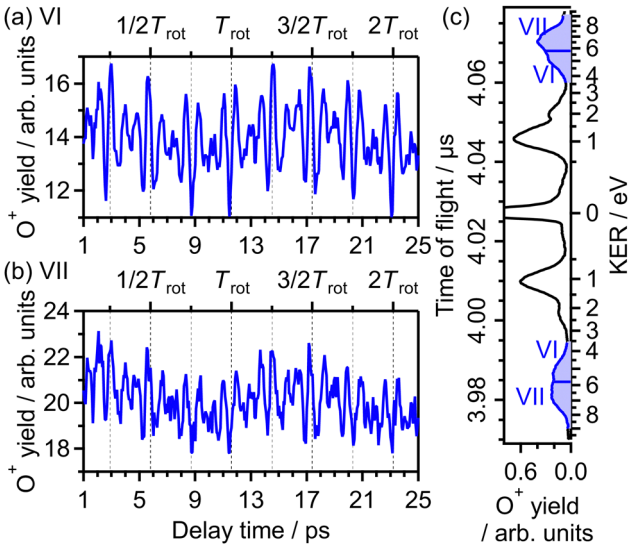

Fig. 15 Recorded O^+ yields as a function of delay time in the energy ranges (a) VI and (b) VII. (c) TOF spectrum obtained only by the probe pulse [same as in Fig. 1(a)] with the labels of the energy ranges VI and VII.

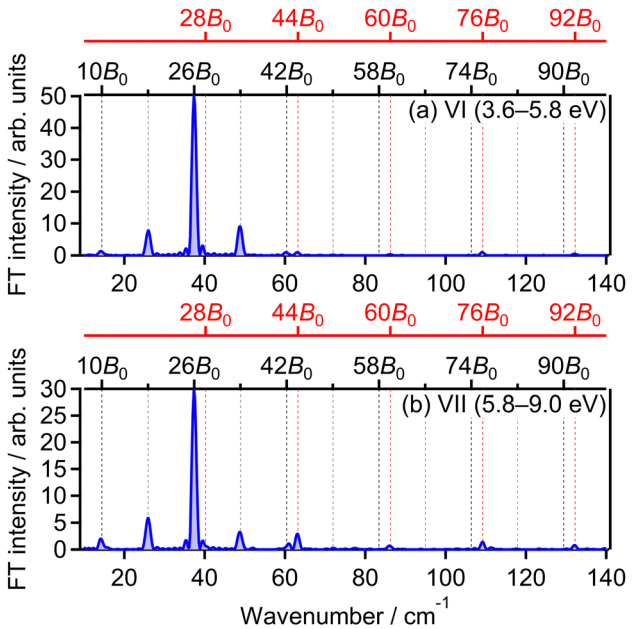

Fig. 16 Fourier transform of O^+ yield in energy ranges (a) VI and (b) VII.

similar character to the (1,0) dissociation in the energy range II. On the other hand, $C_{II,VII}$ is found to be 69%, indicating that the delay dependence of the O^+ yield in the energy range VII is different from that in the range II. Fig. 16(a) and (b) show the FT spectrum of the delay dependence the O^+ yield in the energy range VI, $Y_{VI}(\tau)$, and that in the range VII, $Y_{VII}(\tau)$, respectively. The peaks assigned to $\Delta N = 4$ components are found to be enhanced for the energy range VII.

On the basis of previous studies on one-photon double ionization of O_2[63,64] and double ionization of O_2 in intense laser fields,[65,66] the peak at $E_{KER} = 7$ eV in the energy range VII can be assigned to the dissociation of O_2^{2+} in the $W^3\Delta_u$ state. The major electron configuration of the $W^3\Delta_u$ state is $1\pi_u^{-1}1\pi_g^{-1}$ (ref. 65) and the electron may not be emitted from the $3\sigma_g$ orbital. This means that the observed delay dependence of the O^+ yield in the energy range VII originates not from the angle-dependent ionization probability but from the O_2 axis distribution itself at the moment of the electron emission because the dissociation rapidly proceeds and the PIA effect for the double ionization is small at the current laser-field intensity.[48]

Meanwhile, in the previous studies on double ionization of O_2 in intense sub-10-fs laser fields,[65,66] no O^+ signal was found in the energy range VI. In addition, in the previous studies on one-photon double ionization of O_2,[63,64] no assignment for direct dissociation from O_2^{2+} was proposed for the O^+ signal in the energy range VI. In ref. 40, the TOF spectrum of O^+ was recorded under a similar experimental condition with the laser temporal duration of 100 fs, and the O^+ signal in the energy range VI was observed. Therefore, O^+ in the energy range VI is produced only when the pulse duration is much longer than 10 fs, suggesting that O^+ originates from enhance ionization[67] associated with elongation of the O_2^+ internuclear distance. From the similarity in the delay dependence of the O^+ yield to that in the energy range II, we consider that the enhanced ionization occurs in the course of the net-two photon dissociation [eqn (14)] after the electron emission from the $3\sigma_g$ orbital.

4 Conclusions

In summary, we examined the dissociative ionization dynamics of O_2 molecules, by recording the delay-dependent O^+ fragment ion yields associated with the time evolution of the rotational wave packet of O_2 created by the pump laser pulse. From the recorded rotational revival patterns, we securely revealed that an electron is emitted from the $1\pi_u$ orbital in the released kinetic energy ranges I (0.05–0.40 eV), III (1.04–1.70 eV) and V (2.40–3.40 eV), and from the $3\sigma_g$ orbital in the energy ranges II (0.50–1.04 eV) and IV (1.80–2.40 eV). The observed released kinetic energy distribution is well understood on the basis of the above-threshold dissociation structure associated with the electron emission from the $1\pi_u$ and $3\sigma_g$ orbitals.

Due to the experimental configuration, only the O^+ fragment ion emitted along the laser polarization direction can be detected in this experiment. However, we observed the yield enhancement of O^+ emitted from the anti-aligned O_2 associated with the electron emission from the $1\pi_u$ orbital. This means that the post-ionization alignment (PIA) of the O_2^+ molecular axis is induced by the probe pulse in the course of dissociation. We estimated the effect of the PIA of the O_2^+ axis induced by the probe pulse by performing the classical trajectory Monte-Carlo simulation incorporating the light-dressed potential picture. For the energy range I, which is assigned to the bond-softening type dissociation associated with the f $^4\Pi_g$–a $^4\Pi_u$ one-photon crossing, we confirmed that the PIA is induced effectively so

that the O^+ fragment ion is emitted along the laser polarization direction.

We also performed the simulation for the electron emission from the $3\sigma_g$ orbital, and found that the effect of the PIA is less effective in the three-photon above-threshold dissociation (energy range IV) than in the net-two photon dissociation (energy range II) associated with the c $^4\Sigma_u^-$–b $^4\Sigma_g^-$ three-photon and one-photon crossings. This result indicates that not only the angle-dependent ionization probability but also the dissociation dynamics can be encoded in the delay-dependent fragment ion yield recorded by the pump–probe measurement.

Author contributions

Shinichi Fukahori: methodology, investigation, formal analysis, software, writing – original draft, funding acquisition. Ayumi Kubo: investigation, data curation, formal analysis. Hirokazu Hasegawa: conceptualization, methodology, writing review & editing, supervision, project administration, funding acquisition.

Data availability

Data for this article, including the delay dependence of the TOF spectrum recorded experimentally, the initial conditions and the results of the CTMC simulations, and the input and output files for the quantum chemical calculations by the GAMESS, are available at Zenodo at **https://doi.org/10.5281/zenodo.12776677**.

Conflicts of interest

There are no conflicts to declare.

Appendices

A Initial conditions in the CTMC simulation

Fig. 17(a) shows the distribution of t_0 for all the 3×10^5 trajectories in the CTMC simulation for the electron emission from the $1\pi_u$ orbital (Section 3.4.1). Because of the nonlinearity of the ionization probability with respect to the laser electric field, the width of the t_0 distribution is narrower than that of the envelope of the laser electric field. The dissociation is defined to occur when r reaches 4 Å in the calculated trajectory and the t_0 distribution of the dissociation trajectories are also shown in Fig. 17(a). On the other hand, Fig. 17(b) shows the distribution of the initial internuclear distance (r_0) at the moment of the electron emission for all the 3×10^5 trajectories. Compared with the Wigner distribution $P_{v=0}(r_0)$, the r_0 distribution is shifted towards the longer internuclear distance because the ionization energy decreases as r becomes larger ($r < 1.4$ Å) [Fig. 6(a)]. However, the dissociation is found to occur only in $r_0 < 1.2$ Å as shown in Fig. 17(b) and we solved the EOM (4) only when $r_0 < 1.25$ Å in this calculation. On the other hand, in the CTMC simulation for the electron emission from the $3\sigma_g$ orbital (Section 3.4.2), we solved the EOM (4) irrespective of the r_0 value.

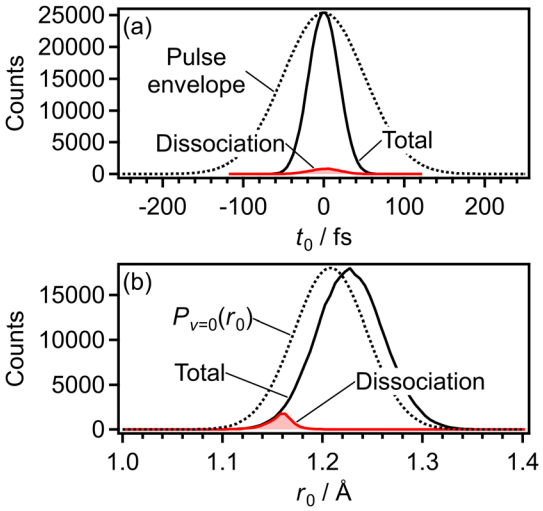

Fig. 17 Initial conditions in the CTMC simulation for the electron emission from the $1\pi_u$ orbital. (a) Distribution of the time of the electron emission, t_0. (b) Distribution of the initial internuclear distance, r_0. Black and red lines represent all the trajectories and the dissociation trajectories, respectively.

B Transition dipole moments and polarizabilities

Transition dipole moments $\mu_t(r)$ as a function of r were obtained by GAMESS 2018 R1[59] at the MCSCF/aug-cc-pVTZ level followed by GUGA[60] along with field-free potential energy curves. Fig. 18(a) and (b) show the resultant transition dipole moments of the f $^4\Pi_g$–a $^4\Pi_u$ and c $^4\Sigma_u^-$–b $^4\Sigma_g^-$ transitions, respectively.

We also obtained the polarizabilities $\alpha_\parallel$ and $\alpha_\perp$ of O_2^+ in the a $^4\Pi_u$ and b $^4\Sigma_g^-$ states as a function of r by the finite-element method as shown in Fig. 19(a)–(d). We found that $\alpha_\parallel$ linearly increases as r increases and $\alpha_\perp$ almost has a constant value in the range of r = 1.2–1.5 Å. We also confirm that the polarizabilities estimated by the energy based method and those estimated by the dipole based method are in agreement with each other in this r range. However, beyond this r range, the agreement of the polarizability between the two methods becomes worse. Therefore, we use linear fit $\alpha_\parallel$ in the range of r and the constant $\alpha_\perp$ value in the entire range of r in this

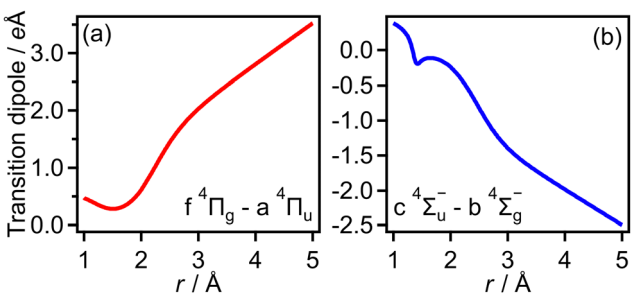

Fig. 18 Calculated dipole moments of (a) f $^4\Pi_g$–a $^4\Pi_u$ transition and (b) c $^4\Sigma_u^-$–b $^4\Sigma_g^-$ transition.

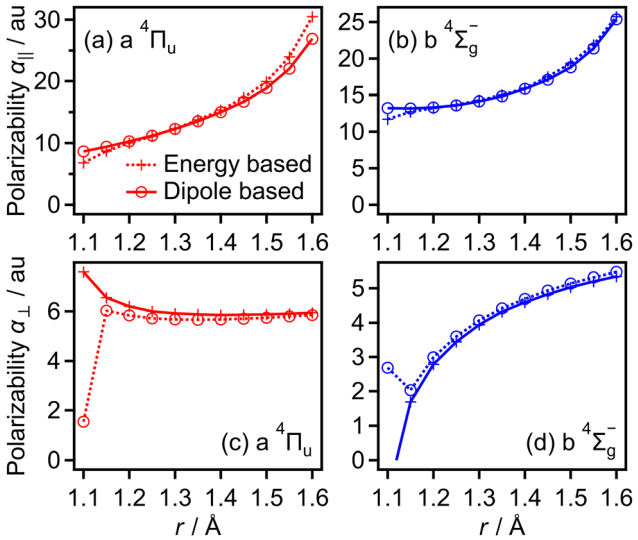

Fig. 19 Calculated polarizabilities of (a) and (c) a $^4\Pi_u$ and (b) and (d) b $^4\Sigma_g^-$ states.

CTMC simulation. For the f $^4\Pi_g$ and c $^4\Sigma_u^-$ states, the agreements between the polarizabilities estimated by the two methods are worse than those for the a $^4\Pi_u$ and b $^4\Sigma_g^-$ states even in the range of r = 1.2–1.5 Å. Considering that the f $^4\Pi_g$ and c $^4\Sigma_u^-$ states are populated in the larger r range where it is hard to calculate the polarizabilities, we used the polarizabilities of O_2^+ in the a $^4\Pi_u$ and b $^4\Sigma_g^-$ states instead of those in the f $^4\Pi_g$ and c $^4\Sigma_u^-$ states, respectively.

Acknowledgements

This work was supported by JSPS KAKENHI Grant Numbers JP17K05593, JP21K18143, JP23H01918, JP23K13705 and JP23K26611 and by the Precise Measurement Technology Promotion Foundation (PMTP-F).

Notes and references

1 K. Codling and L. J. Frasinski, *J. Phys. B: At., Mol. Opt. Phys.*, 1993, **26**, 783–809.
2 J. H. Posthumus, *Rep. Prog. Phys.*, 2004, **67**, 623–665.
3 A. Giusti-Suzor, X. He, O. Atabek and F. H. Mies, *Phys. Rev. Lett.*, 1990, **64**, 515–518.
4 P. H. Bucksbaum, A. Zavriyev, H. G. Muller and D. W. Schumacher, *Phys. Rev. Lett.*, 1990, **64**, 1883–1886.
5 A. Zavriyev, P. H. Bucksbaum, H. G. Muller and D. W. Schumacher, *Phys. Rev. A: At., Mol., Opt. Phys.*, 1990, **42**, 5500–5513.
6 A. Zavriyev, P. H. Bucksbaum, J. Squier and F. Saline, *Phys. Rev. Lett.*, 1993, **70**, 1077–1080.
7 E. E. Aubanel, A. Conjusteau and A. D. Bandrauk, *Phys. Rev. A: At., Mol., Opt. Phys.*, 1993, **48**, R4011–R4014.
8 A. Giusti-Suzor, F. H. Mies, L. F. DiMauro, E. Charron and B. Yang, *J. Phys. B: At., Mol. Opt. Phys.*, 1995, **28**, 309–339.
9 R. Numico, A. Keller and O. Atabek, *Phys. Rev. A: At., Mol., Opt. Phys.*, 1999, **60**, 406–413.
10 L. J. Frasinski, C. R. Courtney and K. Codling, *J. Mod. Opt.*, 2003, **50**, 485–495.
11 M. Uhlmann, T. Kunert and R. Schmidt, *Phys. Rev. A: At., Mol., Opt. Phys.*, 2005, **72**, 045402.
12 I. Heide, L. Catherine, D. B. André, S. André and L. François, *J. Phys. B: At., Mol. Opt. Phys.*, 2018, **51**, 042002.
13 B. K. McFarland, J. P. Farrell, P. H. Bucksbaum and M. Guhr, *Science*, 2008, **322**, 1232–1235.
14 J. P. Farrell, B. K. McFarland, M. Gühr and P. H. Bucksbaum, *Chem. Phys.*, 2009, **366**, 15–21.
15 Y. Mairesse, J. Higuet, N. Dudovich, D. Shafir, B. Fabre, E. Mével, E. Constant, S. Patchkovskii, Z. Walters, M. Y. Ivanov and O. Smirnova, *Phys. Rev. Lett.*, 2010, **104**, 213601.
16 H. J. Wörner, J. B. Bertrand, P. Hockett, P. B. Corkum and D. M. Villeneuve, *Phys. Rev. Lett.*, 2010, **104**, 233904.
17 C. Jin, J. B. Bertrand, R. R. Lucchese, H. J. Wörner, P. B. Corkum, D. M. Villeneuve, A.-T. Le and C. D. Lin, *Phys. Rev. A: At., Mol., Opt. Phys.*, 2012, **85**, 013405.
18 O. Smirnova, Y. Mairesse, S. Patchkovskii, N. Dudovich, D. Villeneuve, P. B. Corkum and M. Y. Ivanov, *Nature*, 2009, **460**, 972–977.
19 J. Yao, G. Li, X. Jia, X. Hao, B. Zeng, C. Jing, W. Chu, J. Ni, H. Zhang, H. Xie, C. Zhang, Z. Zhao, J. Chen, X. Liu, Y. Cheng and Z. Xu, *Phys. Rev. Lett.*, 2013, **111**, 133001.
20 A. S. Alnaser, S. Voss, X. M. Tong, C. M. Maharjan, P. Ranitovic, B. Ulrich, T. Osipov, B. Shan, Z. Chang and C. L. Cocke, *Phys. Rev. Lett.*, 2004, **93**, 113003.
21 T. Kanai, S. Minemoto and H. Sakai, *Nature*, 2005, **435**, 470.
22 D. Pavičić, K. F. Lee, D. M. Rayner, P. B. Corkum and D. M. Villeneuve, *Phys. Rev. Lett.*, 2007, **98**, 243001.
23 H. Akagi, T. Otobe, A. Staudte, A. Shiner, F. Turner, R. Dörner, D. M. Villeneuve and P. B. Corkum, *Science*, 2009, **325**, 1364–1367.
24 P. Simon, V. V. Yulian, S. Alejandro, C. Alberto and D. Piero, *Phys. Rev. Lett.*, 2010, **104**, 223001.
25 J. L. Hansen, L. Holmegaard, J. H. Nielsen, H. Stapelfeldt, D. Dimitrovski and L. B. Madsen, *J. Phys. B: At., Mol. Opt. Phys.*, 2012, **45**, 015101.
26 J. Wu, L. P. H. Schmidt, M. Kunitski, M. Meckel, S. Voss, H. Sann, H. Kim, T. Jahnke, A. Czasch and R. Dörner, *Phys. Rev. Lett.*, 2012, **108**, 183001.
27 X. Xie, K. Doblhoff-Dier, H. Xu, S. Roither, M. S. Schöffler, D. Kartashov, S. Erattupuzha, T. Rathje, G. G. Paulus, K. Yamanouchi, A. Baltuška, S. Gräfe and M. Kitzler, *Phys. Rev. Lett.*, 2014, **112**, 163003.
28 H. Hasegawa, Y. Ikeda, K. Sonoda, T. Sato, A. Iwasaki and K. Yamanouchi, *Chem. Phys. Lett.*, 2016, **662**, 235–239.
29 P. Sándor, A. Sissay, F. Mauger, P. M. Abanador, T. T. Gorman, T. D. Scarborough, M. B. Gaarde, K. Lopata, K. J. Schafer and R. R. Jones, *Phys. Rev. A*, 2018, **98**, 043425.
30 H. V. S. Lam, S. Yarlagadda, A. Venkatachalam, T. N. Wangjam, R. K. Kushawaha, C. Cheng, P. Svihra, A. Nomerotski, T. Weinacht, D. Rolles and V. Kumarappan, *Phys. Rev. A*, 2020, **102**, 043119.

31 T. N. Wangjam, H. V. S. Lam and V. Kumarappan, *Phys. Rev. A*, 2021, **104**, 043112.
32 S. Fukahori, A. Iwasaki, K. Yamanouchi and H. Hasegawa, *J. Chem. Phys.*, 2022, **156**, 094307.
33 I. Kikuchi, S. Fukahori and H. Hasegawa, *Phys. Rev. A*, 2023, **108**, 013101.
34 S. Fukahori, I. Kikuchi and H. Hasegawa, *Chem. Phys. Lett.*, 2023, **833**, 140912.
35 H. Stapelfeldt and T. Seideman, *Rev. Mod. Phys.*, 2003, **75**, 543–557.
36 T. Seideman and E. Hamilton, *Adv. At., Mol., Opt. Phys.*, 2005, **52**, 289–329.
37 Y. Ohshima and H. Hasegawa, *Int. Rev. Phys. Chem.*, 2010, **29**, 619–663.
38 C. P. Koch, M. Lemeshko and D. Sugny, *Rev. Mod. Phys.*, 2019, **91**, 035005.
39 H. Hu, Y. Hung, S. Larimian, S. Erattupuzha, A. Baltuška, M. Zeiler and X. Xie, *Front. Phys.*, 2022, **10**, 1076671.
40 A. Hishikawa, S. Liu, A. Iwasaki and K. Yamanouchi, *J. Chem. Phys.*, 2001, **114**, 9856–9862.
41 S. De, M. Magrakvelidze, I. A. Bocharova, D. Ray, W. Cao, I. Znakovskaya, H. Li, Z. Wang, G. Laurent, U. Thumm, M. F. Kling, I. V. Litvinyuk, I. Ben-Itzhak and C. L. Cocke, *Phys. Rev. A: At., Mol., Opt. Phys.*, 2011, **84**, 043410.
42 A. Sen, T. Sairam, S. R. Sahu, B. Bapat, R. Gopal and V. Sharma, *J. Chem. Phys.*, 2020, **152**, 014302.
43 H. Liu, S.-F. Zhao, M. Li, Y. Deng, C. Wu, X.-X. Zhou, Q. Gong and Y. Liu, *Phys. Rev. A: At., Mol., Opt. Phys.*, 2013, **88**, 061401.
44 J. Yu, X. Yu, X. Zhao, Z. Yin, X. Li, P. Ma, C. Wang, S. Luo and D. Ding, *J. Phys. B: At., Mol. Opt. Phys.*, 2020, **53**, 085601.
45 O. Edqvist, E. Lindholm, L. E. Selin and L. Åsbrink, *Phys. Scr.*, 1970, **1**, 25.
46 A. M. Sayler, P. Q. Wang, K. D. Carnes, B. D. Esry and I. Ben-Itzhak, *Phys. Rev. A: At., Mol., Opt. Phys.*, 2007, **75**, 063420.
47 M. Zohrabi, J. McKenna, B. Gaire, N. G. Johnson, K. D. Carnes, S. De, I. A. Bocharova, M. Magrakvelidze, D. Ray, I. V. Litvinyuk, C. L. Cocke and I. Ben-Itzhak, *Phys. Rev. A: At., Mol., Opt. Phys.*, 2011, **83**, 053405.
48 X. M. Tong, Z. X. Zhao, A. S. Alnaser, S. Voss, C. L. Cocke and C. D. Lin, *J. Phys. B: At., Mol. Opt. Phys.*, 2005, **38**, 333–341.
49 A. Hishikawa, A. Iwamae, K. Hoshina, M. Kono and K. Yamanouchi, *Chem. Phys.*, 1998, **231**, 315–329.
50 E. Wigner, *Phys. Rev.*, 1932, **40**, 749–759.
51 X. M. Tong, Z. X. Zhao and C. D. Lin, *Phys. Rev. A: At., Mol., Opt. Phys.*, 2002, **66**, 033402.
52 S.-F. Zhao, C. Jin, A.-T. Le, T. F. Jiang and C. D. Lin, *Phys. Rev. A: At., Mol., Opt. Phys.*, 2010, **81**, 033423.
53 Y. Khodorkovsky, K. Kitano, H. Hasegawa, Y. Ohshima and I. S. Averbukh, *Phys. Rev. A: At., Mol., Opt. Phys.*, 2011, **83**, 023423.
54 C. Ellert and P. B. Corkum, *Phys. Rev. A: At., Mol., Opt. Phys.*, 1999, **59**, R3170–R3173.
55 I. Maruyama, T. Sako and K. Yamanouchi, *J. Phys. B: At., Mol. Opt. Phys.*, 2004, **37**, 3919–3936.
56 J. C. Tully and R. K. Preston, *J. Chem. Phys.*, 1971, **55**, 562–572.
57 J. W. C. Johns and D. W. Lepard, *J. Mol. Spectrosc.*, 1975, **55**, 374–406.
58 K. Sonoda, S. Fukahori and H. Hasegawa, *Phys. Rev. A*, 2021, **103**, 033118.
59 G. M. J. Barca, C. Bertoni, L. Carrington, D. Datta, N. D. Silva, J. E. Deustua, D. G. Fedorov, J. R. Gour, A. O. Gunina, E. Guidez, T. Harville, S. Irle, J. Ivanic, K. Kowalski, S. S. Leang, H. Li, W. Li, J. J. Lutz, I. Magoulas, J. Mato, V. Mironov, H. Nakata, B. Q. Pham, P. Piecuch, D. Poole, S. R. Pruitt, A. P. Rendell, L. B. Roskop, K. Ruedenberg, T. Sattasathuchana, M. W. Schmidt, J. Shen, L. Slipchenko, M. Sosonkina, V. Sundriyal, A. Tiwari, J. L. G. Vallejo, B. Westheimer, M. Włoch, P. Xu, F. Zahariev and M. S. Gordon, *J. Chem. Phys.*, 2020, **152**, 154102.
60 M. Magrakvelidze, C. M. Aikens and U. Thumm, *Phys. Rev. A: At., Mol., Opt. Phys.*, 2012, **86**, 023402.
61 T. Tanaka, H. Yoshii, Y. Morioka, T. Hayaishi, K. Ito and R. I. Hall, *J. Chem. Phys.*, 1998, **108**, 6240–6248.
62 J. H. D. Eland and E. J. Duerr, *Chem. Phys.*, 1998, **229**, 1–11.
63 M. Lundqvist, D. Edvardsson, P. Baltzer, M. Larsson and B. Wannberg, *J. Phys. B: At., Mol. Opt. Phys.*, 1996, **29**, 499.
64 S. Hsieh and J. H. D. Eland, *J. Phys. B: At., Mol. Opt. Phys.*, 1996, **29**, 5795.
65 S. Voss, A. S. Alnaser, X. M. Tong, C. Maharjan, P. Ranitovic, B. Ulrich, B. Shan, Z. Chang, C. D. Lin and C. L. Cocke, *J. Phys. B: At., Mol. Opt. Phys.*, 2004, **37**, 4239–4257.
66 S. De, I. A. Bocharova, M. Magrakvelidze, D. Ray, W. Cao, B. Bergues, U. Thumm, M. F. Kling, I. V. Litvinyuk and C. L. Cocke, *Phys. Rev. A: At., Mol., Opt. Phys.*, 2010, **82**, 013408.
67 W. Lai and C. Guo, *Phys. Rev. A*, 2016, **93**, 043401.

